# Slab Rollback Orogeny model: A test-of-concept

**Luca Dal Zilio**[1,2*], **Edi Kissling**[1], **Taras Gerya**[1], **Ylona van Dinther**[1,3]

[1] Department of Earth Sciences, ETH Zürich, Sonneggstrasse 5, 8092 Zürich, Switzerland
[2] Seismological Laboratory, California Institute of Technology, Pasadena, California
[3] Department of Earth Sciences, Utrecht University, The Netherlands

**Abstract**

Forces associated with subduction of cold and dense oceanic plates control the motions and deformations of convergent margins. However, how these forces sustain mountain building processes — especially after slab breakoff — is still poorly known. Here we investigate this conundrum by performing 2-D, visco-elasto-plastic, seismo-thermo-mechanical numerical modeling, which simulates both tectonic and seismicity processes in a subduction and continental collision setting. Results reproduce the self-driven stages of subduction, continental collision, and spontaneous slab breakoff. The subsequent evolution of the orogen shows how slow, but persistent, flexural bending of post-breakoff residual slab and crustal delamination control the post-collisional evolution of the orogen. This so-called *Slab Rollback Orogeny* model leads to bending-related slab suction, nappe stacking of the crustal root, widening of the orogen, and a seismicity pattern consistent with the different tectonic regimes throughout the orogen. Our results provide an explanation for the post-collisional evolution of the Central Alps and its current seismicity.

## 1 Introduction

The process of continent-continent collision in shaping mountain ranges and adjacent foreland basins has been discussed over many decades (e.g., Beaumont et al., 1996; Malinverno and Ryan, 1986; Uyeda and Kanamori, 1979). According to the most commonly used conceptual models, the evolution of mountain belts is largely driven by the horizontal convergence between the two colliding plates (e.g., Handy et al., 2010; Schmid et al., 1996). This view is based on the perception in which a rigid indenter — frequently exemplified by a bulldozer — converts kinematic convergence into mountain building (e.g., Willett, 2010, for a review). These mechanisms have been used to explain the accretion of crustal material from the upper and lower plates onto the orogen, the construction of topography, and the erosional recycling of the accreted material (e.g., Beaumont et al., 1996; Whipple, 2009).

Similar kinematic assumptions can potentially be applied to the Alpine orogeny to investigate crustal accretion and surface erosional processes on both the orogen and the adjacent foreland basins. However, recent studies have shown that this approach does not predict two first-order observations at deeper crustal levels and on the surface. In particular, these include (*i*) a >50% underestimate of the depth of the crust-mantle transition (i.e., Moho) beneath the core of the mountain range, and (*ii*) an overestimate of the mean surface elevation if principles of isostatic equilibrium were properly considered (Kissling and Schlunegger, 2018). This has particularly been the case in the Central Alps (Fig. 1a), where the crustal root has been seismically deter-

* Corresponding author: Luca Dal Zilio, dalzilio@caltech.edu

mined to be ∼60-km thick, and thus far out of conventional isostatic equilibrium with a mean surface topography of only ∼2 km (Kissling, 1993). A more recent, alternative explanation suggests that the Central Alps evolved in response to a slab rollback process, in which the dynamic buoyancy forces of a retreating subduction are the major driving forces of the orogenic system (e.g., Brun and Faccenna, 2008; Royden, 1993). This alternative model of the post-collisional Alpine evolution, which we refer to as *Slab Rollback Orogeny* (SRO) model, is based on the well-known concepts of slab pull and retreat, force balancing, and the principles of mass conservation (e.g., Heuret and Lallemand, 2005; Malinverno and Ryan, 1986; Royden, 1993; Schellart, 2008). The SRO model provides a dynamically consistent mechanism to explain the construction of thick sedimentary successions in the Molasse basin where the extra slab load has maintained the Alpine surface at moderate, but persistent, elevations (Schlunegger and Kissling, 2015). Furthermore, it offers an explanation for the architecture of the crustal root, which comprises an imbricate stack of lower crustal material derived from the subducting European plate (Fry et al., 2010).

On a large-scale, teleseismic tomography cross-sections have shown that, along the NW–SE transect across the Central Alps, the slab dips with only ∼60° (Fig. 1b), while along a N–S transect at ∼10°E longitude the slab hangs in a sub-vertical position beneath the core of the Alps (Lippitsch et al., 2003). Furthermore, a recent review of different high-resolution tomographic studies combined with shear- and body-wave models show that at depths of 250 km, the slab in the Central Alps becomes indistinguishable, thus leading to the conclusion that a breakoff is likely at a depth of roughly 250 km (Kästle et al., 2019). If the scenario proposed by Lippitsch et al. (2003) holds, the SRO model might offer an explanation for the current seismicity pattern across the Central Alps (Fig. 1c), which is characterized by bending-related normal-faulting events within the subducting European plate (Singer et al., 2014).

Thus far, numerical models of subduction have widely been used to study, e.g., force interactions between the upper and lower plates (e.g., Capitanio et al., 2010; Faccenda et al., 2009; Magni et al., 2014; van Dinther et al., 2010), continental collision processes (e.g., Faccenda et al., 2008; Pusok et al., 2018), sedimentation (e.g., Erdős et al., 2019), as well as the breakoff process and its consequences on the evolution of topography, stress field and magmatism (e.g., Duretz et al., 2011; Magni et al., 2013; van Hunen and Allen, 2011). However, less work has been done in studying the post-collisional dynamics. In particular, the open question is whether the buoyancy forces are capable of sustaining the retreat process of a collisional orogen, even after slab breakoff. In this study, we employ a newly-developed, high-resolution (400 m), 2-D seismo-thermo-mechanical (STM) model to simulate both the long-term tectonic and the short-term seismicity of a generic convergent margin, from subduction to collisional orogeny. Our focus is on the self-consistent dynamics where driving and resisting forces are balanced with plate motions and deformations. This allows understanding of (*i*) the force propagation from the lower plate to the upper plate and the controls on the stress regime and (*ii*) the impact of the dynamics on the tectonic and seismicity style of plate motions. Lastly, we discuss the possible applications of our model to the Central Alps collision system.

## 2 Seismo-Thermo-Mechanical modeling

We employ the 2-D, continuum-based, finite difference code I2ELVIS (Gerya and Yuen, 2007). Extensions for seismo-thermo-mechanical modeling are validated

and described in van Dinther et al. (2013). This single-framework model uses a fully staggered Eulerian grid in combination with a Lagrangian marker-in-cell technique. We then implicitly solve the conservation of mass, momentum, and heat for an incompressible medium with a visco-elasto-plastic rheology. The momentum equations include the inertial term to stabilize high-coseismic slip rates at low time steps. A time step of 1 years, however, reduces our formulation towards a virtually quasi-static one. Ruptures during the resulting events hence represent the occurrence of rapid threshold-exceeding slip during which permanent displacement and stress drop occur along a localized interface.

The brittle/plastic faulting process is simulated by a Drucker-Prager plastic yielding model in which the second invariant of the deviatoric stress tensor is limited at each Lagrangian rock marker by a pressure-dependent yield stress. Brittle instabilities and subsequent healing are introduced by a strongly rate-dependent friction formulation (e.g., Ampuero and Ben-Zion, 2008), in which the effective friction coefficient $\mu_{eff}$ depends on the visco-plastic slip velocity $V = (\sigma_{yield}/\eta_m)\Delta x$, in which $\eta_m$ is the local viscosity from the previous time step and $\Delta x$ is the Eulerian grid size:

$$\mu_{eff} = \frac{V_c\,\mu_s \;+\; V\,\mu_d}{V_c + V}\;; \tag{1}$$

where $\mu_s$ and $\mu_d$ are static and dynamic friction coefficients, respectively, $V_c$ is the characteristic velocity, namely the velocity at which half of the friction change has occurred, and $\gamma$ represents the amount of slip velocity-induced weakening if $\gamma = 1 - (\mu_d/\mu_s)$ is positive, or strengthening if $\gamma$ is negative. This local, invariant formulation allows for spontaneous localization at any orientation. The spontaneous rupture paths are governed by local stress and strength states instead of being a priori defined.

The initial model domain consists of two continental plates separated by an oceanic basin (Fig. 2a and S1). The dimensions of the model box is 3000 x 1200 km$^2$ (1921 x 347 nodes), and all the mechanical boundaries are free slip. Variable grid spacing enables to reach a 400 m grid resolution in the central part of the domain where the continental collision takes place. The initial conditions of the model are built during the initial stage of kinematic convergence. During this period, the oceanic subduction is kinematically prescribed using internal kinematic constrains (5 cm/yr until 200 km of shortening is accommodated). After this model initialization step, the internal kinematic constrain is removed and the model is driven by internal, buoyancy forces. In this way, the obtained thermo-mechanical state is employed as the initial condition for a self-driven, retreating subduction and continental collision. The subduction and collision rates, which are not in steady state, are controlled by the contribution of slab pull, crustal buoyancy, and dissipative forces. We employ an additional 20 km thick layer of sticky air ($\eta_{air} = 10^{18}$ Pa s, $\rho_{air} = 1$ kg/m$^3$) to mimic the effect of a free surface and enable the development of topography (Crameri et al., 2012). The visco-elasto-plastic thermo-mechanical parameters of each lithology are based on a range of laboratory experiments (Table S1). An extended description of the numerical technique, model setup, and modeling procedure is given in the Supporting Information.

# 3 Results

## 3.1 Stage 1: Subduction, collision, and slab breakoff

After an initial stage of kinematically imposed subduction initiation, oceanic lithosphere sinks spontaneously at the ocean-upper plate continental margin. Self-sustaining retreating subduction causes the migration of the trench and exerts a suction force to the upper continental plate, while the subduction-induced mantle flow maintains the upper plate highly coupled with the retreating slab (Fig. 2b,c). Toward the onset of continental collision, sediments are accreted in the orogenic prism, while the upper plate acts as a buttress. The buoyancy of the continental crust slows down subduction and, hence, the convergence, though a non-negligible part of continental lithosphere is still being subducted. The collisional zone thus achieves an asymmetric architecture with a doubly-vergent thrusting pattern. Slab necking occurs at a relatively shallow depth of approximately 250 km during the stage of slab steepening (Fig. S2). Breakoff occurs at the ocean-continent transition a few million years after the collision stage initiated. Slab breakoff and subsequent rebound produces a sharp topographic signal, which results in an uplift rate of $\sim$0.5 mm/yr due to a rebound of $\sim$5 km in $\sim$10 My. Such uplift is modulated by the rate of removal of overburden by erosional processes. A simulation example is shown in Supplementary Movie S1.

## 3.2 Stage 2: Post-collisional slab rollback evolution of the orogen

Our numerical experiments indicate that the removal of the oceanic lithospheric slab after slab breakoff is responsible for a stress redistribution within the lithosphere. Partial release of the gravitational stresses during breakoff is followed by the unbending of the remaining slab and a localized increase of stress in the lower plate related to the positive buoyancy of the subducted continental crust. However, our numerical simulations show that the vertical slab pull force — offered by the remaining slab — remains the dominant driving force in the collisional system (Fig. 3a and S3). Following the rapid transient visco-elastic rebound after slab breakoff, the continued flexural bending of the lower plate provokes the migration of the whole orogen towards the foreland basin (Fig. S3). The ongoing rollback collision triggers crustal delamination in the lower plate and shortening at shallower crustal levels, and thus results in the uplift of the frontal part of the orogen and in the foreland basin. At deeper crustal levels, extrusion and stacking of buoyant crustal materials occur on the downgoing plate, while the remaining crust continues to subduct at a low, but detectable, sinking rate (Fig. 3a). In addition, heating of the slab decreases the flexural strength of the foreland plate. This process increases the curvature of the subducted plate, thereby reaching deeper levels in the asthenosphere closer to a thermoelastic relaxation of a continental plate to applied loads.

## 3.3 Stage 3: Regional stresses and seismicity distribution

Results from the seismic cycle simulations show a wide domain subjected to brittle faulting. Seismogenic deformation in the orogenic wedge is largely driven by extensional stresses resulting from the development of retreating subduction (Fig. 3b and S3). Because of the yielding of the upper plate, the orogenic wedge partially overthrusts the retro-foreland domain. High compressional stresses are transferred on the upper plate, thus causing a development of a sequence of seismogenic thrusts at the front and beneath the retro-foreland basin (Fig. 3b). Deep earthquakes beneath the foreland basin extend into the lower crust and their distribution correlates well with the

flexural bending of the gently to steeply dipping downgoing plate. Flexural bending thus transfers stresses into the lithosphere beneath the foreland basin. Such a tectonic stress transfer leads to a locally enhanced regional stress field in the lower and upper crust beneath the foreland with a compressional component in the shallower domains and an extensional domain at deeper crustal levels (Fig. 4). The laterally variable rheological contrasts between the deeper crustal roots and the brittle shallow crust explain the depth dependency of the seismicity pattern. Lastly, these results illustrate how the long-term tectonic evolution and crustal properties affect the architecture of the orogen and thereby their short-term spatial distribution of seismicity.

## 4 Discussion

### 4.1 Mountain building processes: Horizontal vs. Vertical Forces

Our results show that vertical buoyancy forces control the dynamic evolution of a post-collisional margin, even in the absence of any pre-imposed convergence between two continental plates. Despite a significant decrease in slab pull force after slab breakoff, flexural bending of the remaining slab is still capable of controlling the post-collisional retreat of the entire orogen (Fig. 3a). Consequently, the construction of an orogen with a pronounced topography and a stack of crustal material is maintained over a longer time period.

The upper and lower plates are mechanically coupled as stresses propagate across the plate boundary (Fig. 4a,b and S3). Compressive and extensional stresses occur simultaneously across the orogen and at different depth levels. Within the lithospheric mantle, horizontal stresses propagate from the lower plate to the upper plate (Fig. 4a). The lower plate is subjected to an in-plane force that depends only on the slab pull. Such in-plane force is then responsible for the flexural bending of the lower plate. The resulting lithospheric flexure leads to extensional stresses with the bending region, while large suction forces propagate across the plate interface triggering compressional stress within the lower plate (Fig. 4b). At shallower crustal levels, horizontal stresses are generally lower. Notably, the underlying dynamics results in a compression-extension-compression regime. Intra-orogenic extension is ascribed to a combination of delamination and extrusion of the crustal roots and gravity-driven orogenic relaxation due to topographic load. As a result, compressional stresses propagate on both the pro-foreland and retro-foreland basins.

Our results indicate that, when the crust remains coupled to the downgoing slab, large buoyancy forces are generated. When these deep crustal domains are warmed up, they decouple from the downgoing slab and are subjected to buoyant extrusion and delamination (Fig. 4b and S3). According to our results, the propagation of the foreland front, coeval with a pervasive crustal delamination — ductile at depth and brittle at shallower levels — suggest a predominant importance of the vertical slab load force. This is accomplished through a combined effect of slab sinking and delamination of the crustal material as a consequence of bending-related suction force and heating of the deep crust. More importantly, these processes create a positive feedback as delamination of buoyant crustal material from the subducting plate increases the relative importance of the vertical slab load, thus promoting further down warping of the plate. Also, this mechanism localizes extensional stresses both at the Moho and within the lower crust (Fig. 4b), with the consequence of intra-crustal seismicity at both shallow and deep crustal levels (Fig. 3b).

### 4.2 Slab Rollback Orogeny Model for the tectonic evolution of the Central Alps

Over the last decades, the building of the European Alps has often been discussed in a kinematic framework (e.g., Handy et al., 2010; Rosenberg et al., 2015; Schmid et al., 1996). Several models of orogeny build on this concept in which the stacking of tectonic nappes and the buildup of topography relate to compressional forces at work in response to the collision between Eurasia and the Adria microplate. This concept considers the kinematic convergence between both the lower and upper plate as the major driver of orogenesis, while the vertical forces — exerted by slab pull and buoyant crustal roots — have generally been neglected.

A comparison between the model here presented and the Central Alps shows some interesting similarities at the scale of the orogen. The dynamic evolution of our model is consistent with palaeomagnetic evidence that the lower (European) continental plate has remained nearly stationary since the Late Cretaceous, and it did not advance during the Alpine orogeny (Dewey et al., 1989). Our model reproduces this large-scale dynamics, in which the convergence of the upper (Adria) plate is solely fueled by slab pull. The post-collisional convergence rate is relatively small (2-3 mm/yr; Fig. 4b and S3), and in agreement with continuous GPS measurements (Calais et al., 2002). The orogenic volume is mostly accommodated on the lower continental plate, with a maximum topography greater than 5 km in height. Finally, at ca. 20 Myr after slab breakoff, crustal shortening propagates towards the foreland basin, similarly to the main shortening observed in the Jura thrust belt over the last 10 Ma (e.g., Burkhard, 1990).

In terms of the detailed architecture of the orogen, the presented modeling results are largely simplified compared to the much more complicated Alpine system. In nature, tectonic processes occur within a three-dimensional (e.g., Pusok et al., 2018), geometrically complex fault system with various scales of down-dip and along-strike variations in its rheology and structure (e.g., Magni et al., 2017). Also, subduction zone interaction (e.g., Király et al., 2016) and magmatism (e.g., Menant et al., 2016) likely affect the distribution of the differential forces, and are lacking in our numerical experiments. However, is important to stress that small-scale complexities of a natural system, like the Alpine orogen, are difficult to reproduce in a self-consistent lithospheric-scale model. Moreover, even excluding along-strike variations of the Alpine arc, details of each individual tectonic structure cannot be expected to be reproduced in a self-driven, generic model such as the ones of this study. On the other hand, the advantage of this model setup is the possibility of simulating a generic convergent margin, and analyzing the long-term forces and seismo-thermo-mechanical behavior acting on the system. In spite of these limitations, the number of salient but enigmatic features that our models do succeed in reproducing and predicting is highly encouraging and provides useful insights.

## 5 Conclusions

The modeling results presented here suggest that post-collisional slab rollback processes are capable of controlling the seismotectonic evolution of collisional orogens. These results demonstrate that, even after slab breakoff, vertical buoyancy forces can lead to horizontal compressional forces through the entire evolution of a convergent margin, from oceanic subduction to continent-continent collision. Such persistent retreating mechanism yields an orogeny-foreland basin ensemble where subsidence and

thrusting are partly decoupled at the scale of the orogeny. Thus, this so-called *Slab Rollback Orogeny* model offers a unifying concept to explain the ensemble of surface and deep lithosphere observations (Kissling and Schlunegger, 2018).

Despite our generic model setup, comparison between our results and the central European Alps reveals some interesting similarities at the scale of the orogen. Based on our numerical experiments, supported by a chronological pattern of crustal deformation (Schlunegger and Kissling, 2015) and on seismic tomography (Fry et al., 2010), we conclude that a *Slab Rollback Orogeny* model is capable to explain (1) the stacking of nappes, (2) the growth of the buoyant crustal root, (3) the evolution of the Molasse foreland basin, and (4) the current extensional seismicity pattern in the central European Alps (Singer et al., 2014). These results contrast with the previously published view on the collisional development of the Alps mainly because in our physics-based numerical model, crustal uplift, nappe stacking, and the buildup of topography are solely driven by buoyancy forces, slab rollback, and the mechanical strength of the subducting plate. In light of these results, while the Himalayas serves as much better examples where mountain building processes are driven by the horizontal push of the subducting plate (i.e., advancing subduction), the understanding of the geologic history of the Central Alps does require an alternative view.

## Acknowledgments

This study was funded by the SNSF Swiss Alp-Array SINERGIA and the Drinkward Fellowship at Caltech (L.D.Z.). Numerical simulations were performed on ETH cluster Euler. This paper benefited from discussions with B. Kaus, G. Pozzi, K. Ueda, and A. Ceccato.

## 6 Methods

### 6.1 Numerical code description

In order to simulate the dynamics of mountain building processes coupled to mantle dynamics, we employ the seismo-thermo-mechanical (STM) van Dinther et al. (2013). This numerical code solves for the two-dimensional steady state momentum equations and heat conservation equation using the finite-difference/marker-in-cell method on a Eulerian grid Gerya and Yuen (2007):

$$\frac{\partial v_x}{\partial x} + \frac{\partial v_z}{\partial z} = 0\,; \tag{2}$$

$$\frac{\partial \sigma'_{xx}}{\partial x} + \frac{\partial \sigma'_{xz}}{\partial z} - \frac{\partial P}{\partial x} = \rho \frac{Dv_x}{Dt}\,; \tag{3}$$

$$\frac{\partial \sigma'_{zz}}{\partial z} + \frac{\partial \sigma'_{zx}}{\partial x} - \frac{\partial P}{\partial z} = \rho \frac{Dv_z}{Dt} - \rho g\,. \tag{4}$$

These equations are solved to obtain the horizontal and vertical velocities ($v_x$ and $v_z$) and pressure ($P$, defined as the mean stress), whereas $\rho$ is density, $\sigma'_{ij}$ are deviatoric stress tensor components, and $g = 9.81\ m/s^2$ is the vertical component of the gravitation acceleration. The advection of transport properties including viscosity, plastic strain and temperature is performed with the displacement of Lagrangian markers.

The momentum equations include the inertial term to stabilize higher slip rates at low time steps. A time step of 1 year, however, reduces our formulation to a virtually

quasi-static one. Ruptures during the resulting events hence represent the occurrence of rapid threshold-exceeding slip during which permanent displacement and stress drop occur along a localized interface.

The heat equation describes the balance of heat in a continuous medium and is solved in a Lagrangian manner and is expressed in the following way Gerya (2010):

$$\rho C_p \frac{DT}{Dt} = -\frac{\partial q_x}{\partial x} - \frac{\partial q_z}{\partial z} + H_\mathrm{r} + H_\mathrm{a} + H_\mathrm{s}; \tag{5}$$

$$q_x = -k(T,C)\frac{\partial T}{\partial x}; \tag{6}$$

$$q_z = -k(T,C)\frac{\partial T}{\partial z}; \tag{7}$$

$$H_a = T\alpha\frac{DP}{Dt}\ ; \tag{8}$$

$$H_\mathrm{s} = \sigma'_{ij}\ \dot{\varepsilon}_{ij,\ vp}. \tag{9}$$

This formulation takes into account the effect of radioactive heating ($H_r$), adiabatic heat production/consumption ($H_a$), and shear heating ($H_s$). $DP/Dt$ represents the substantive time derivative of pressure, whereas $\alpha$ is the thermal expansion. Thermal conductivity $k(T,C)$ is a function of both temperature and composition (Table 1). $q_x$ and $q_z$ are the horizontal and vertical components of the heat flux vector, $\dot{\varepsilon}_{ij,\ vp}$ is the visco-plastic component of the deviatoric strain rate tensor. The isobaric heat capacity ($C_p$) and isothermal compression term are computed at each timestep and takes into account the effect of latent heat due to phase transformations Faccenda and Dal Zilio (2017). Evaluation of $H_T$ and $H_s$ terms requires information from the pressure and stress tensor components. These terms are thus computed after solving the Stokes equations. The heat equation can then be solved taking into account the effect of isothermal compression, phases changes and shear heating at the current timestep.

### 6.2 Rheological model

We consider that the strength of the lithosphere is controlled, at the different timescales of orogeny, by the combination of both brittle and ductile deformation mechanisms in a visco-elasto-plastic rheology. Viscous creep is computed in terms of deformation invariants and depends on strain rate, temperature, and pressure Ranalli (1995). The effective viscosity ($\eta_{eff}$) of the deformation is calculated as a combination of diffusion ($\eta_{diff}$) and dislocation creep ($\eta_{dis}$):

$$\frac{1}{\eta_{eff}} = \frac{1}{\eta_{diff}} + \frac{1}{\eta_{disl}}\ . \tag{10}$$

The calculation of the viscosity associated with dislocation creep regime is formulated as follows:

$$\eta_{disl} = \frac{1}{2}\ A_d\ \sigma\prime_{II}^{1-n}\ exp(\frac{E_a + PV_a}{nRT})\ , \tag{11}$$

where $\sigma\prime_{II}$ is the second invariant of deviatoric stress tensor, $A_d$ is the pre-exponential factor, $E_a$ the activation energy, $V_a$ is the activation volume, $n$ the stress exponent,

and $R$ is the gas constant. Those material properties are determined from laboratory flow experiments and are given in Table 1.

Dislocation creep is dominant for high stress levels, while diffusion creep is a thermally activated mechanism and is the most convenient way to accommodate deformation at low stress conditions:

$$\eta_{diff} = \frac{1}{2} A_d \, \tau_{tr}^{1-n} \, exp(\frac{E_a + PV_a}{nRT}). \tag{12}$$

In this case, $\tau_{tr}$ defines the stress transition between diffusion creep and dislocation creep, which is assumed to occur at 30 kPa Turcotte and Schubert (2002).

Our rheological model takes into account a second semi-brittle deformation mechanism characterized by the exponential flow of olivine and also known as Peierls mechanism. As demonstrated in Duretz et al. (2011), Peierls creep in olivine is a key mechanism for slab breakoff, generally causing slabs to break earlier and at shallower depths. This flow mechanism has been put in evidence in a number experimental studies Evans and Goetze (1979); Katayama and Karato (2008). Moreover, recent studies have shown that the existence of plate tectonics requires sufficiently lithospheric yield stress that are lower than Mohr–Coulomb stresses Van Heck and Tackley (2008). Such conditions necessitate the use of stress limiters such as Peierls creep which promotes the localization of deformation in the lithospheric mantle Kameyama et al. (1999); Lu et al. (2011). The effective viscosity corresponding to the Peierls creep regime is characterized by an exponential dependance on the second stress invariant and is formulated as:

$$\eta_{peierls} = \frac{1}{2A_{peierls}\sigma_{II}} exp\left(\frac{E_a + PV_a}{nRT}\left(1 - \left(\frac{\sigma_{II}}{\sigma_{peierls}}\right)^p\right)^q\right). \tag{13}$$

For dry olivine, $A_{peierls} = 10^{7.8}\ 10^{-12}\ Pa^{-2}s^{-1}$ is the material constant for Peierls creep, $\sigma_{peierls}$ is the Peierls stress that limits the strength of the material and corresponds to 9.1 GPa Evans and Goetze (1979). Exponents $p$ and $q$ depend on the shape and geometry of obstacles that limit the dislocation motion and are equal to 1 and 2, respectively. The Peierls mechanism is a dominant deformation mechanism of the downgoing slab, where the temperature is low and stress is high Karato et al. (2001).

The 2-D steady state momentum equations are solved using constitutive relations that relate deviatoric stresses and strain rates in a nonlinear visco-elasto-plastic manner:

$$\dot{\varepsilon_{ij}} = \frac{1}{2G}\frac{D\sigma'_{ij}}{Dt} + \frac{1}{2\eta}\sigma'_{ij} + \begin{cases} 0 & \text{for } \sigma'_{II} < \sigma_{yield} \\ \chi\frac{\partial\sigma'_{II}}{\partial\sigma'_{ij}} = \chi\frac{\partial\sigma'_{ij}}{2\sigma'_{II}} & \text{for } \sigma'_{II} = \sigma_{yield} \end{cases} \tag{14}$$

where $G$ is shear modulus and $\eta$ is effective viscosity. $D\sigma'_{ij}/Dt$ is the objective co-rotational time derivative solved using a time explicit scheme Gerya (2010) and $\sigma_{II} = \sqrt{{\sigma'_{xx}}^2 + {\sigma'_{xz}}^2}$ is the second invariant of the deviatoric stress tensor, and $\chi$ is a plastic multiplier connecting plastic strain rates and stresses. Introducing a visco-plastic viscosity ($\eta_{vp}$), we can rewrite eq. 14 as:

$$\sigma'_{ij} = 2\eta_{vp} Z \dot{\varepsilon_{ij}} + \sigma_{ij}(1 - Z) \tag{15}$$

where $Z$ is the visco-elasticity factor:

$$Z = \frac{G\Delta t_{comp}}{G\Delta t_{comp} + \eta_{vp}} \tag{16}$$

where $\Delta t_{comp}$ is the computational time step.

The brittle part of the lithosphere is controlled by Mohr–Coulomb (or non-associative Drucker-Prager) plasticity which expresses the linear dependence of the geomaterials resistance on the total pressure Prager and Drucker (1952). Mohr–Coulomb plasticity acts as a stress limiter in the regions where the second stress invariant ($\sigma_{ii}$) exceeds the material yield stress. The yield stress depends on the pressure, the standard strength (i.e., cohesion) $C$, and the effective friction coefficient $\mu_{eff}$:

$$\sigma_{yield} = C + \mu_{eff}\, P\,. \tag{17}$$

An important component in the yield criterion is the friction coefficient. Following the approach of van Dinther et al. (2013), we apply a strongly rate-dependent friction formulation Ampuero and Ben-Zion (2008), in which the effective friction coefficient $\mu_{eff}$ depends on the visco-plastic slip velocity $V = (\sigma_{yield}/\eta_m)\Delta x$, in which $\eta_m$ is the local viscosity from the previous time step and $\Delta x$ is the Eulerian grid size:

$$\mu_{eff} = \frac{V_c\,\mu_s \;+\; V\,\mu_d}{V_c + V} \tag{18}$$

$$\gamma = 1 - (\mu_d/\mu_s) \tag{19}$$

where $\mu_s$ and $\mu_d$ are static and dynamic friction coefficients, respectively, $V_c$ is the characteristic velocity, namely the velocity at which half of the friction change has occurred, and $\gamma$ represents the amount of slip velocity-induced weakening if $\gamma = 1 - (\mu_d/\mu_s)$ is positive, or strengthening if $\gamma$ is negative.

When plastic yielding condition is locally reached we require a constant second invariant of deviatoric stresses (assuming the absence of elastic deformation)

$$\text{if} \quad \sigma'_{II} = \sigma_{yield} : \left\{ \quad \frac{D\sigma'_{II}}{Dt} = 0, \quad \dot{\varepsilon_{ij}}^{elastic} = 0 \right\}; \tag{20}$$

then the stress components are similarly (i.e., isotropically) corrected so that

$$\sigma'_{ij} = \sigma'_{ij} \cdot \frac{\sigma_{yield}}{\sigma'_{II}}. \tag{21}$$

Accordingly, the local viscosity-like parameter $\eta_{vp}$ decreases to weaken the material and to localise deformation:

$$\eta_{vp} = \eta \frac{\sigma'_{II}}{\eta\chi + \sigma'_{II}}\,, \tag{22}$$

where:

$$\chi = 2(\dot{\varepsilon_{II}} - \dot{\varepsilon_{II}}^{viscous}) = 2(\dot{\varepsilon_{II}} - \frac{1}{2\eta}\sigma'_{II}) \tag{23}$$

$$\dot{\varepsilon_{II}} = \sqrt{\dot{\varepsilon_{xx}}^2 + \dot{\varepsilon_{xz}}^2}\,. \tag{24}$$

Finally the visco-plastic viscosity $\eta_{vp}$ is corrected during plastic deformation:

$$\eta_{vp} = \frac{\sigma_{yield}}{2\dot{\varepsilon_{II}}}\,. \tag{25}$$

On the other hand, if the plastic yielding condition is not satisfied, this means that the material is under elastic and/or viscous deformation (i.e., diffusion and/or dislocation creep), therefore $\eta_{vp} = \eta$.

### 6.3 Eclogitization

Eclogitization of the continental mafic crust can have major effects on the evolution of continental plates. With the progression of the reaction, the eclogitized continental root becomes denser than the surrounding mantle and thus it is prone to foundering (Kay and Kay, 1993). Numerical models predict that high-density eclogite affects the orogeny evolution Doin and Henry (2001); Li et al. (2016) and, if sufficiently weak, can lead to delamination of the continental plate Krystopowicz and Currie (2013). Eclogitization of subducted crustal material is here implemented in a relatively simplified manner Faccenda and Dal Zilio (2017). More specifically, for the basalts of the upper and lower mafic crust, a phase transition from basalt to garnet-granulite and then eclogite Ito and Kennedy (1971) is applied. Eclogitization of the crust is implemented as a linear density increase with pressure and temperature from 0% to 16% in the P–T region between the experimentally determined garnet-in and plagioclase-out phase transitions in basalt Ito and Kennedy (1971). For temperatures lower than $T_{ecl_{min}}$ = 673K no eclogitization is possible. For temperatures between $T_{ecl_{min}}$ and $T_{ecl_{max}}$= 873 K the maximum density increase due to eclogitization is linearly increasing with temperature from 0% to 16%.

### 6.4 Estimation of Moment Magnitude ($M_W$)

During the seismic cycle simulation we analyze all rupture events to determine their downdip rupture width ($W$). These events occurring throughout the orogen are recognized using a Rupture Detector Algorithm (RDA), which analyzes each Lagrangian marker in space and time throughout the simulation Dal Zilio et al. (2018). If its velocity exceeds a threshold of 9.0 x $10^{-9}$ m $s^{-1}$, while simultaneously stresses drop more than 0.4 MPa that marker's physical properties are stored in a synthetic data set. Subsequently markers are grouped into one event when they occur within 400 m of a marker that ruptured this or the previous time step. The rationale for choosing these thresholds comes from the minimally common stress drop Allmann and Shearer (2009) and our Eulerian grid size of 400 m, respectively.

From these spontaneous rupture paths we measure the rupture width ($W$) to estimate the moment magnitude ($M_W$) using the empirical scaling relations in Wells and Coppersmith (1994). This empirical relationship is available from regression analysis based on a large numbers of events in nature:

$$M_W = a + b\, log\,(W), \tag{26}$$

where $a$ and $b$ are coefficients that vary with the style-of-faulting (i.e., normal or reverse faulting). We chose Wells and Coppersmith (1994) because they include various types of faulting and different tectonic environments.

### 6.5 Setup

The initial model domain consists of two continental plates separated by an oceanic basin (see Fig. 1a). The dimensions of the model box is 3000 x 1200 $km^2$ (1921 x 347 nodes), and all the mechanical boundaries are free slip. Variable grid spacing enables to reach a 400 m grid resolution in the central part of the domain where the continental collision takes place. Lithological structure are resolved with ∼33 million markers. In order to study the interplay between subduction and orogenic evolution, we follow the semi-dynamic approach employed in Duretz et al. (2011). The initial conditions of the model are built during the initial stage of kinematic conver-

gence. During this period, the oceanic subduction is kinematically prescribed using internal kinematic constrains (5 cm/yr until 200 km of shortening is accommodated). With ongoing convergence, the upper plate decouple from the lateral sides of the box; this zones accommodate hot mantle upwellings and are therefore the location where oceanic ridges spontaneously develop. After this model initialization step, the internal kinematic constrain is removed and the model is driven by internal, buoyancy forces. Thus, the obtained thermo-mechanical state is employed as the initial condition for a self-driven, retreating subduction and continental collision. The subduction and collision rates, which are not in steady state, are controlled by the contribution of slab pull, crustal buoyancy, and dissipative forces. We employ an additional 20 km thick layer of sticky air ($\eta_{air} = 10^{18}$ Pa s, $\rho_{air} = 1$ kg/m$^3$) in order to mimic the effect of a free surface and enable the development of topography Crameri et al. (2012).

The thermal structure of the oceanic lithosphere was calculated from the half space cooling model for a given plate age Turcotte and Schubert (2002) using a slab age of 70 Ma and a diffusivity of $10^{-6}$ m$^2$ s$^1$. The initial continental geotherm is defined as a linear temperature variation from the model surface (T=293 K) to the lithosphere–asthenosphere boundary (T=1617.6 K), the left and right sides of the model domain are insulating boundaries. The geothermal gradient in the asthenospheric mantle below the lithosphere is 0.5 K/km (Fig. 1c).

In order to initiate subduction a weak zone was imposed on the right ocean–upper plate transition. The weak zone cuts through the whole lithospheric mantle with an angle of $\sim$30° and is characterized by weak plastic strength (1 MPa) and wet olivine rheology Ranalli (1995). Despite the fact that subduction initiation can be modelled in a geologically more relevant manner Nikolaeva et al. (2010), the use of such a weak zone remains useful for our specific setup.

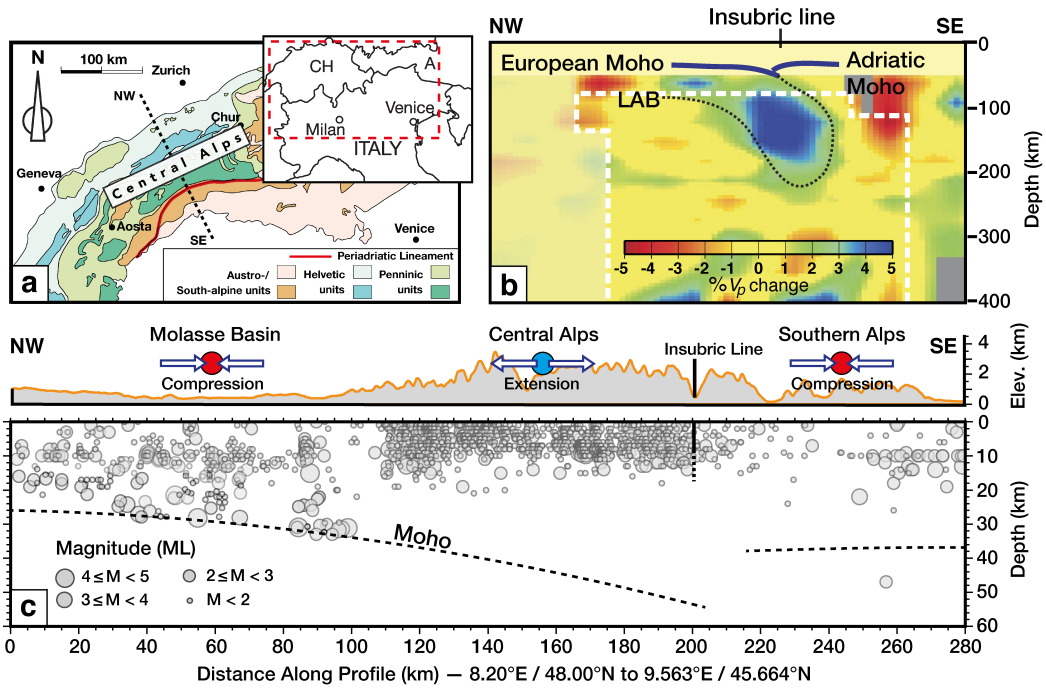


**Figure 1.** **a**, Inset map illustrating the Alps and its foreland basin along with the section discussed in this study. **b**, Teleseismic tomography cross-section illustrating the geometry of the European slab beneath the central Alps. The figure shows lateral variations of P-wave velocity Vp beneath the Moho. **c**, Topographic signal and vertical cross-section approximately perpendicular to the strike of the Central Alps. Transparent gray circles represent hypocenters. Dashed black lines indicate the Moho with a ±3 km uncertainty of the depth (Spada et al., 2013).

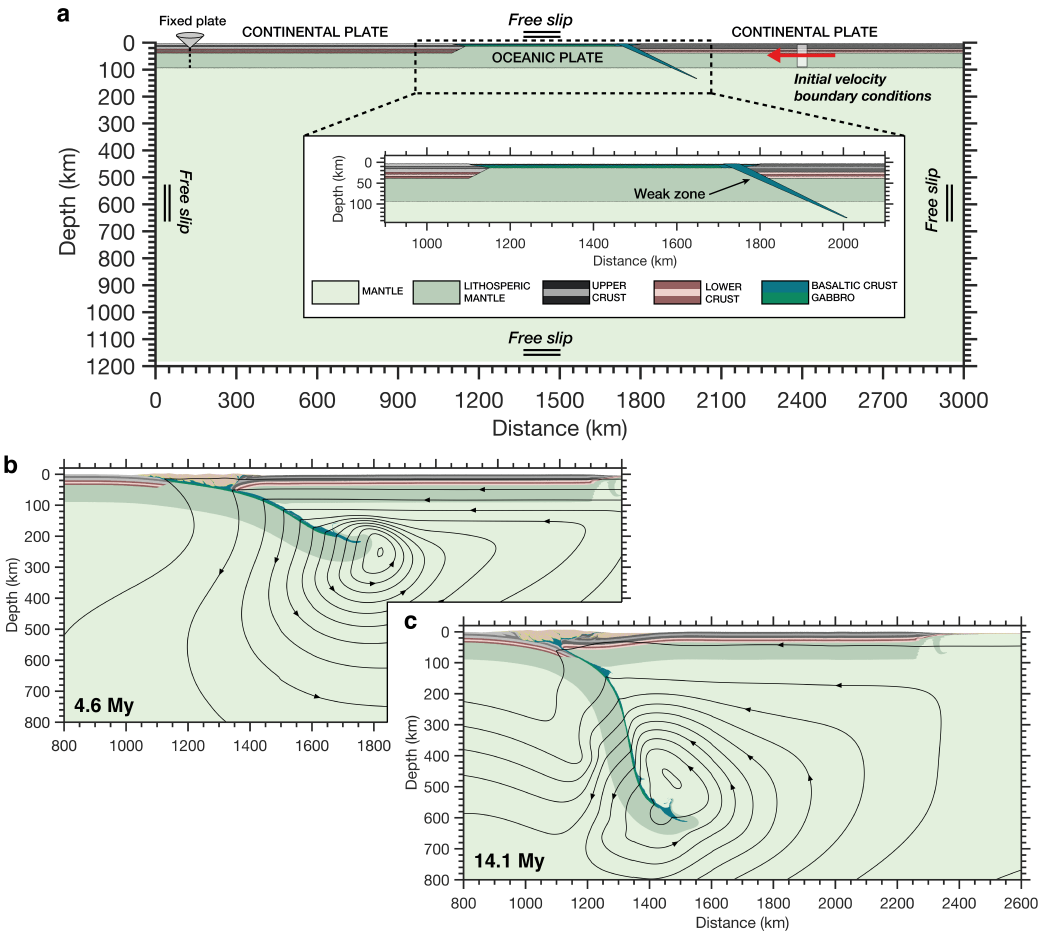


**Figure 2.** **a**, 2-D initial setup. Initial composition map including boundary conditions. The model simulates subduction initiation through the use of a fixed convergence rate on the upper plate until ∼200 km of oceanic crust has been subducted. For this initial period only, plate convergence rate is applied at 2500 km on the right (upper) plate (red arrow). Zoom shows the oceanic plate and pre-imposed weak zone to initiate subduction. **b**–**c**, Dynamic evolution of a spontaneously retreating subducting plate. Key stages of mantle-lithosphere interaction after 4.6 and 14.1 My. The superimposed stream function contours display the effect of subduction-induced trench suction and return flow in mantle, which maintain the upper plate coupled with the retreating slab.

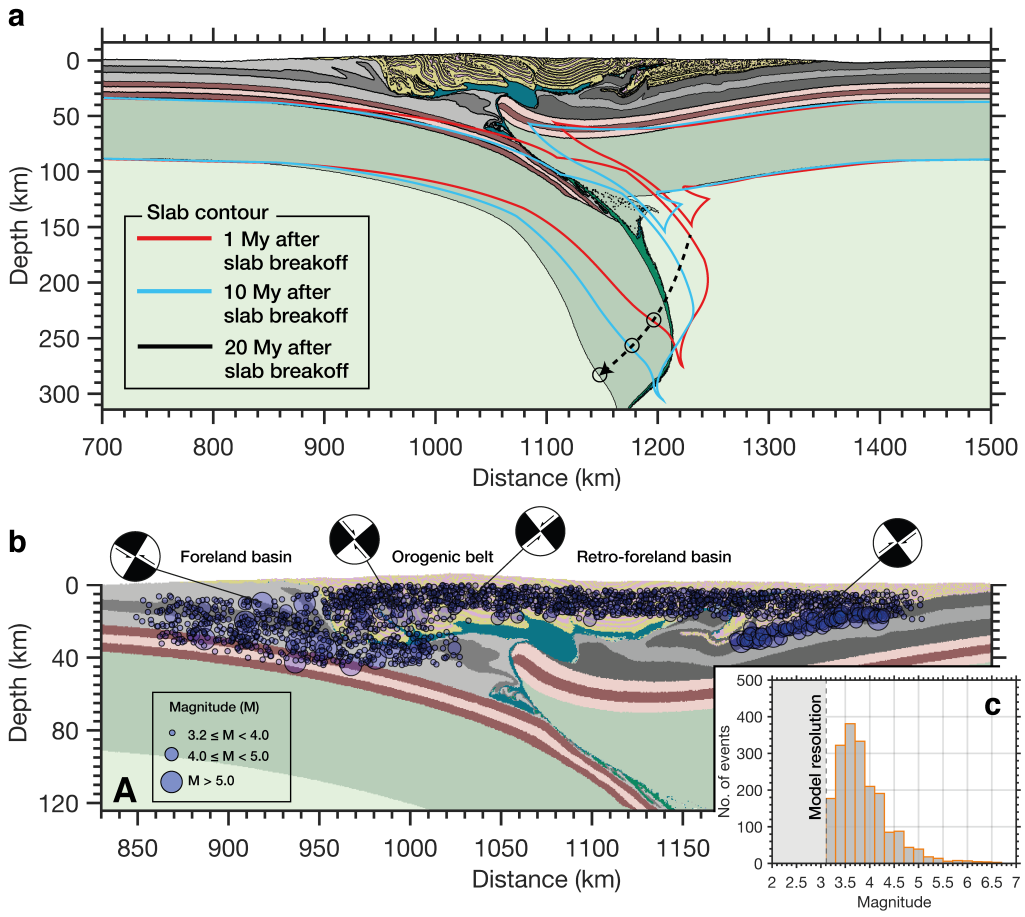


**Figure 3.** **a**, Post-collisional evolution with superimposed contours of the slab geometries at 1 and 10 My after slab breakoff. Compositional map shows the final structure 20 My after slab breakoff. Evolution of the orogen is driven by slow slab rollback and delamination of crustal material. **b**, Short-term seismicity pattern of the reference model. Cluster of seismicity and the inferred 2-D focal mechanisms display a broad pattern of different style of faulting, which are consistent with the local tectonic regime. **c**, Histograms of all events and the corresponding magnitude.

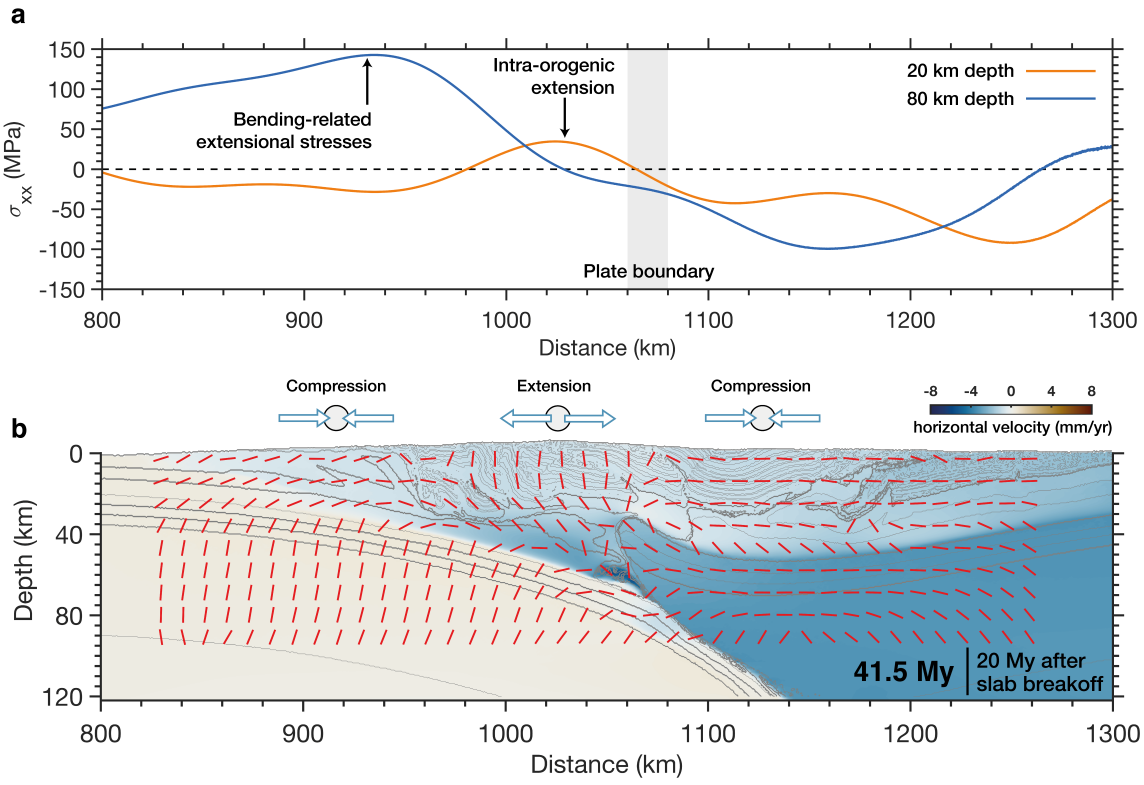


**Figure 4.** **a**, Horizontal stress throughout the orogen. Stress is measured at 20 and 80 km depth at the time of 41.5 My. Positive is extension, negative is compression. In the bending area stresses are reoriented and not parallel to the horizontal. **b**, Color scale shows the spatial distribution of horizontal velocity ($V_x$). Red bars indicate orientations of maximum (compression) principal stresses. The inferred stress axes show a broad pattern of different tectonic regimes (compression-extension-compression), which are consistent with the style of faulting and seismicity pattern.

| *Material* *flow law* [a] | $\rho_0$ [b] ($kg\ m^{-3}$) | $E_a$ [a] ($kJ\ mol^{-1}$) | $V_a$ [a] ($J/bar$) | $n$ [a] | $\eta_0$ [a] ($Pa^n\ s$) | $Hr$ [b,c] ($\mu W m^{-3}$) | $k$ [a] $Wm^{-1}K^{-1}$ | $G$ ($GPa$) | $\mu_s$ [d,e,f] | $\lambda$ [g,h] |
|---|---|---|---|---|---|---|---|---|---|---|
| Sediments (Wet Qz) | 2600 | 154 | 1.2 | 2.3 | 1.97 x $10^{17}$ | 1.5 | $[0.64 + 807/(T + 77)]$ $exp(4\ 10^{-5}P)$ | 25 | 0.35 | 0.4 |
| Upper cont. crust (Wet Qz) | 2750 | 154 | 0.8 | 2.3 | 1.97 x $10^{17}$ | 0.25 | $[0.64 + 807/(T + 77)]$ $exp(4\ 10^{-5}P)$ | 34 | 0.6 | 0.4 |
| Lower cont. crust (Mafic Granulite) | 3000 | 445 | 0.8 | 4.2 | 1.25 x $10^{21}$ | 1.5 | $[0.64 + 807/(T + 77)]$ $exp(4\ 10^{-5}P)$ | 34 | 0.6 | 0.4 |
| Upper oc. crust (Wet Qz) | 3000 | 154 | 0.8 | 2.3 | 1.97 x $10^{17}$ | 0.25 | $[1.18 + 974/(T + 77)]$ $exp(4\ 10^{-5}P)$ | 38 | 0.6 | 0.95 |
| Lower oc. crust (Plg-An 75%) | 3300 | 238 | 0.8 | 3.2 | 4.8 x $10^{22}$ | 0.0022 | $[1.18 + 974/(T + 77)]$ $exp(4\ 10^{-5}P)$ | 38 | 0.6 | 0.4 |
| Mantle (Dry Olivine) | 3300 | 532 | 0.8 | 3.5 | 3.98 x $10^{16}$ | 0.0022 | $[0.73 + 1293/(T + 77)]$ $exp(4\ 10^{-5}P)$ | 67 | 0.6 | 0.4 |

**Table 1.** Rheological parameters. $\rho_0$ is the reference density, $E_a$ is the activation energy, $V_a$ is the activation volume, $n$ is the stress exponent, $\eta_0$ is the reference viscosity, $Hr$ is the radiogenic heat production, $G$ is the shear modulus, $\mu_s$ is the static friction coefficient and $\lambda$ is the pore-fluid pressure factor ($P_{fluid}/P_{solid}$). Other properties for all rock types: cohesion ($C$) is 1 MPa Schultz (1995), specific heat capacity ($C_p$) is 1000 $J\ kg^{-1}K^{-1}$, thermal conductivity ($k$) is in $Wm^{-1}K^{-1}$ at $T_K$ and $P_{MPa}$, thermal expansion $\alpha_\rho$= 3x$10^{-5}$ $K^{-1}$ and compressibility $\beta_\rho$=1x$10^{-5}$ $MPa^{-1}$. [a] Ranalli (1995); [b] Turcotte and Schubert (2002); [c] Rudnick and Fountain (1995); [d] Di Toro et al. (2011); [e] Del Gaudio et al. (2009); [f] Den Hartog et al. (2012); [g] Sibson (1994); [h] Seno (2009).

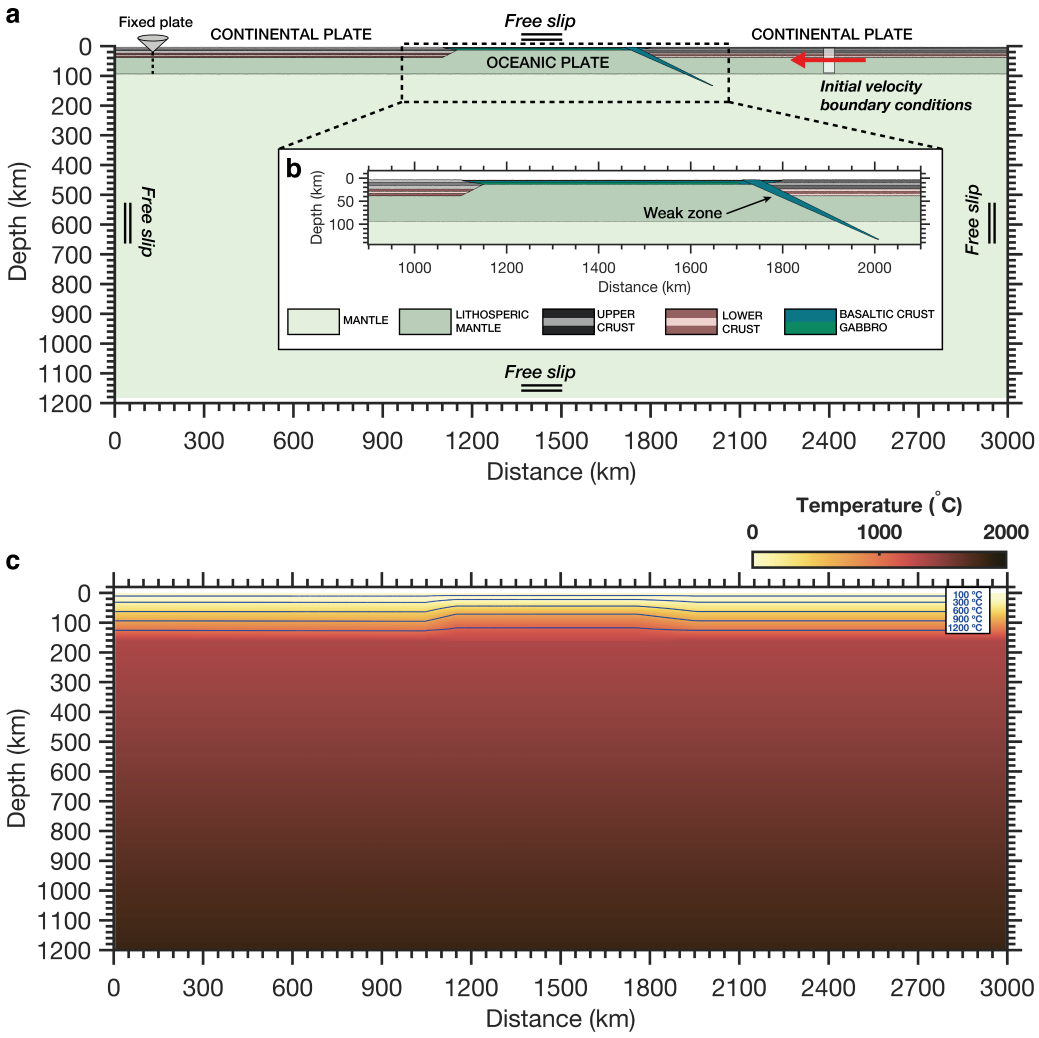


**Figure S1.** 2-D initial setup. **a**, Initial composition map including boundary conditions. **b**, Zoom of oceanic plate and pre-imposed weak zone to initiate subduction. The model simulates subduction initiation through the use of a fixed convergence rate on the upper plate until ∼200 km of oceanic crust has been subducted. Plate convergence rate is applied at 2500 km on the right (upper) plate (red arrow). **c**, Initial temperature distribution.

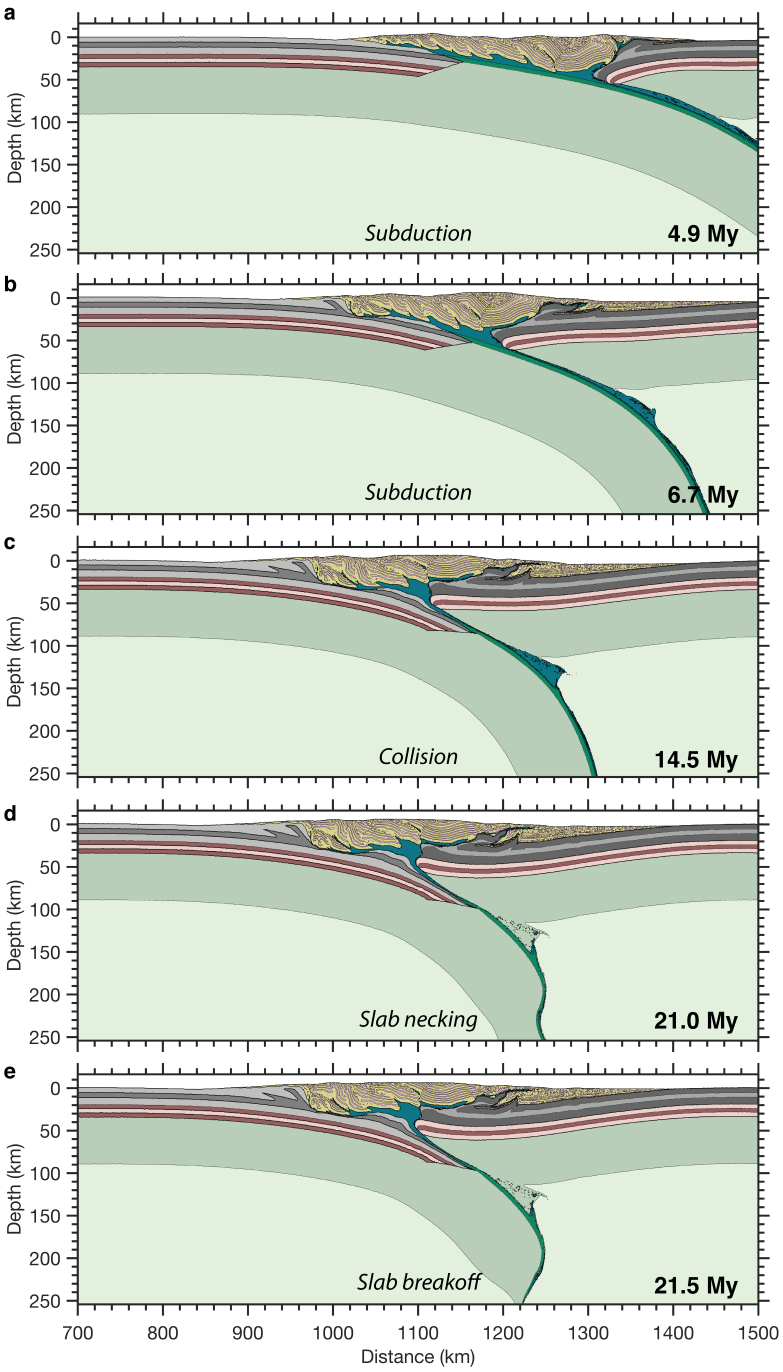


**Figure S2.** Long-term evolution of subduction (**a**–**b**), collision (**c**), slab necking (**d**), and slab breakoff (**e**). The early phases of the models consist of oceanic plate consumption and ocean closure. The collisional regime is greatly affected by the buoyant and rheologically weak materials entering the subduction channel from above. The final structure is that of a *coupled* collision system.

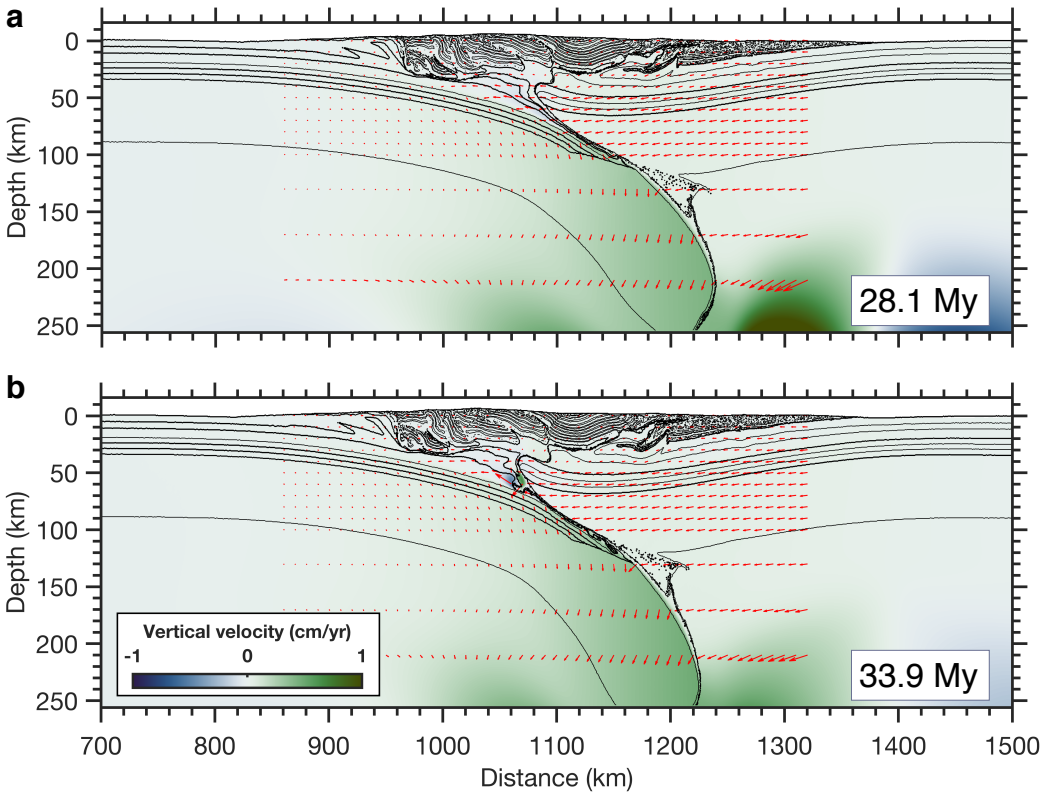


**Figure S3.** Vertical velocity field in color overlain by arrows indicating velocities at 28.1 (∼7 My after slab breakoff) and 33.9 (∼13 My after slab breakoff) My. The inferred velocity fields show how the vertical sinking of the post breakoff remaining slab translates into horizontal convergence of the upper plate and uplift in the core of the orogen.

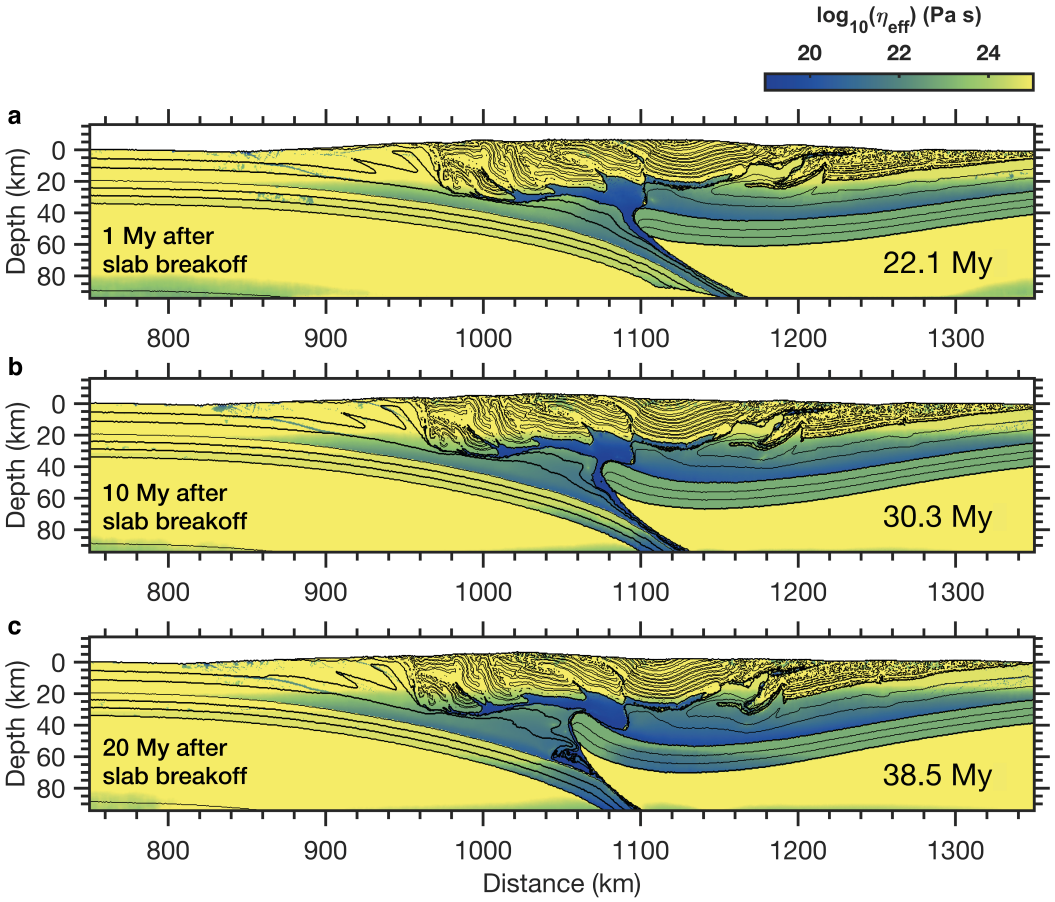


**Figure S4.** Viscosity field at 1 My (**a**), 10 My (**b**), and 20 My (**c**) after slab breakoff. The rheological contrasts between the deeper lower crust and the brittle high strength shallow crust illustrate how the long-term tectonic evolution and crustal properties affect the architecture of the orogen and thereby their short-term spatial distribution of seismicity shown in Fig. 3b.

## References


Allmann, B. P. and Shearer, P. M. (2009). Global variations of stress drop for moderate to large earthquakes. *Journal of Geophysical Research: Solid Earth*, 114(B1).

Ampuero, J.-P. and Ben-Zion, Y. (2008). Cracks, pulses and macroscopic asymmetry of dynamic rupture on a bimaterial interface with velocity-weakening friction. *Geophysical Journal International*, 173(2):674–692.

Beaumont, C., Ellis, S., Hamilton, J., and Fullsack, P. (1996). Mechanical model for subduction-collision tectonics of alpine-type compressional orogens. *Geology*, 24(8):675–678.

Brun, J.-P. and Faccenna, C. (2008). Exhumation of high-pressure rocks driven by slab rollback. *Earth and Planetary Science Letters*, 272(1-2):1–7.

Burkhard, M. (1990). Aspects of the large-scale miocene deformation in the most external part of the swiss alps (sub-alpine molasse to jura fold belt). *Eclogae Geologicae Helvetiae*, 83(3):559–583.

Calais, E., Nocquet, J.-M., Jouanne, F., and Tardy, M. (2002). Current strain regime in the western alps from continuous global positioning system measurements, 1996–2001. *Geology*, 30(7):651–654.

Capitanio, F., Stegman, D., Moresi, L.-N., and Sharples, W. (2010). Upper plate controls on deep subduction, trench migrations and deformations at convergent margins. *Tectonophysics*, 483(1):80–92.

Crameri, F., Schmeling, H., Golabek, G., Duretz, T., Orendt, R., Buiter, S., May, D., Kaus, B., Gerya, T., and Tackley, P. (2012). A comparison of numerical surface topography calculations in geodynamic modelling: An evaluation of the 'sticky air'method. *Geophysical Journal International*, 189(1):38–54.

Dal Zilio, L., van Dinther, Y., Gerya, T. V., and Pranger, C. C. (2018). Seismic behaviour of mountain belts controlled by plate convergence rate. *Earth and Planetary Science Letters*, 482:81–92.

Del Gaudio, P., Di Toro, G., Han, R., Hirose, T., Nielsen, S., Shimamoto, T., and Cavallo, A. (2009). Frictional melting of peridotite and seismic slip. *Journal of Geophysical Research: Solid Earth*, 114(B6).

Den Hartog, S., Niemeijer, A., and Spiers, C. (2012). New constraints on megathrust slip stability under subduction zone p–t conditions. *Earth and Planetary Science Letters*, 353:240–252.

Dewey, J., Helman, M., Knott, S., Turco, E., and Hutton, D. (1989). Kinematics of the western mediterranean. *Geological Society, London, Special Publications*, 45(1):265–283.

Di Toro, G., Han, R., Hirose, T., De Paola, N., Nielsen, S., Mizoguchi, K., Ferri, F., Cocco, M., and Shimamoto, T. (2011). Fault lubrication during earthquakes. *Nature*, 471(7339):494–498.

Doin, M.-P. and Henry, P. (2001). Subduction initiation and continental crust recycling: the roles of rheology and eclogitization. *Tectonophysics*, 342(1-2):163–191.

Duretz, T., Gerya, T. V., and May, D. A. (2011). Numerical modelling of spontaneous slab breakoff and subsequent topographic response. *Tectonophysics*, 502(1-2):244–256.

Erdős, Z., Huismans, R. S., and Beek, P. v. d. (2019). Control of increased sedimentation on orogenic fold-and-thrust belt structure–insights into the evolution of the western alps. *Solid Earth*, 10(2):391–404.

Evans, B. and Goetze, C. (1979). The temperature variation of hardness of olivine and its implication for polycrystalline yield stress. *Journal of Geophysical Research: Solid Earth*, 84(B10):5505–5524.

Faccenda, M. and Dal Zilio, L. (2017). The role of solid–solid phase transitions in mantle convection. *Lithos*, 268:198–224.

Faccenda, M., Gerya, T. V., and Chakraborty, S. (2008). Styles of post-subduction collisional orogeny: influence of convergence velocity, crustal rheology and radiogenic heat production. *Lithos*, 103(1):257–287.

Faccenda, M., Minelli, G., and Gerya, T. (2009). Coupled and decoupled regimes of continental collision: Numerical modeling. *Earth and Planetary Science Letters*, 278(3-4):337–349.

Fry, B., Deschamps, F., Kissling, E., Stehly, L., and Giardini, D. (2010). Layered azimuthal anisotropy of rayleigh wave phase velocities in the european alpine lithosphere inferred from ambient noise. *Earth and Planetary Science Letters*, 297(1-2):95–102.

Gerya, T. (2010). *Introduction to Numerical Geodynamic Modelling*. Cambridge University Press.

Gerya, T. and Yuen, D. (2007). Robust characteristics method for modelling multiphase visco-elasto-plastic thermo-mechanical problems. *Physics of the Earth and Planetary Interiors*, 163(1):83–105.

Handy, M. R., Schmid, S. M., Bousquet, R., Kissling, E., and Bernoulli, D. (2010). Reconciling plate-tectonic reconstructions of alpine tethys with the geological–geophysical record of spreading and subduction in the alps. *Earth-Science Reviews*, 102(3-4):121–158.

Heuret, A. and Lallemand, S. (2005). Plate motions, slab dynamics and back-arc deformation. *Physics of the Earth and Planetary Interiors*, 149(1-2):31–51.

Ito, K. and Kennedy, G. C. (1971). An experimental study of the basalt-garnet granulite-eclogite transition. *The structure and physical properties of the Earth's crust*, 14:303–314.

Kameyama, M., Yuen, D. A., and Karato, S.-I. (1999). Thermal-mechanical effects of low-temperature plasticity (the peierls mechanism) on the deformation of a viscoelastic shear zone. *Earth and Planetary Science Letters*, 168(1-2):159–172.

Karato, S.-i., Riedel, M. R., and Yuen, D. A. (2001). Rheological structure and deformation of subducted slabs in the mantle transition zone: implications for mantle circulation and deep earthquakes. *Physics of the Earth and Planetary Interiors*, 127(1-4):83–108.

Kästle, E. D., Rosenberg, C., Boschi, L., Bellahsen, N., Meier, T., and El-Sharkawy, A. (2019). Slab break-offs in the alpine subduction zone. *Solid Earth Discussions*, 2019:1–16.

Katayama, I. and Karato, S.-i. (2008). Low-temperature, high-stress deformation of olivine under water-saturated conditions. *Physics of the Earth and Planetary Interiors*, 168(3):125–133.

Király, Á., Capitanio, F. A., Funiciello, F., and Faccenna, C. (2016). Subduction zone interaction: Controls on arcuate belts. *Geology*, 44(9):715–718.

Kissling, E. (1993). Deep structure of the alps—what do we really know? *Physics of the Earth and Planetary Interiors*, 79(1-2):87–112.

Kissling, E. and Schlunegger, F. (2018). Rollback orogeny model for the evolution of the swiss alps. *Tectonics*, 37(4):1097–1115.

Krystopowicz, N. J. and Currie, C. A. (2013). Crustal eclogitization and lithosphere delamination in orogens. *Earth and Planetary Science Letters*, 361:195–207.

Li, Z.-H., Liu, M., and Gerya, T. (2016). Lithosphere delamination in continental collisional orogens: A systematic numerical study. *Journal of Geophysical Research: Solid Earth*, 121(7):5186–5211.

Lippitsch, R., Kissling, E., and Ansorge, J. (2003). Upper mantle structure beneath the alpine orogen from high-resolution teleseismic tomography. *Journal of Geophysical Research: Solid Earth*, 108(B8).

Lu, G., Kaus, B. J., and Zhao, L. (2011). Thermal localization as a potential mechanism to rift cratons. *Physics of the Earth and Planetary Interiors*, 186(3-4):125–137.

Magni, V., Allen, M. B., van Hunen, J., and Bouilhol, P. (2017). Continental underplating after slab break-off. *Earth and Planetary Science Letters*, 474:59–67.

Magni, V., Faccenna, C., van Hunen, J., and Funiciello, F. (2013). Delamination vs. break-off: the fate of continental collision. *Geophysical Research Letters*, 40(2):285–289.

Magni, V., Faccenna, C., van Hunen, J., and Funiciello, F. (2014). How collision triggers backarc extension: Insight into mediterranean style of extension from 3-d numerical models. *Geology*, 42(6):511–514.

Malinverno, A. and Ryan, W. B. (1986). Extension in the tyrrhenian sea and shortening in the apennines as result of arc migration driven by sinking of the lithosphere. *Tectonics*, 5(2):227–245.

Menant, A., Sternai, P., Jolivet, L., Guillou-Frottier, L., and Gerya, T. (2016). 3d numerical modeling of mantle flow, crustal dynamics and magma genesis associated with slab roll-back and tearing: The eastern mediterranean case. *Earth and Planetary Science Letters*, 442:93–107.

Nikolaeva, K., Gerya, T., and Marques, F. (2010). Subduction initiation at passive margins: Numerical modeling. *Journal of Geophysical Research: Solid Earth (1978–2012)*, 115(B3).

Prager, W. and Drucker, D. (1952). Soil mechanics and plastic analysis or limit design, 0. *Appi. Math*, 10(2):157–165.

Pusok, A. E., Kaus, B. J., and Popov, A. A. (2018). The effect of rheological approximations in 3-d numerical simulations of subduction and collision. *Tectonophysics*, 746:296–311.

Ranalli, G. (1995). *Rheology of the Earth*. Springer.

Rosenberg, C. L., Berger, A., Bellahsen, N., and Bousquet, R. (2015). Relating orogen width to shortening, erosion, and exhumation during alpine collision. *Tectonics*, 34(6):1306–1328.

Royden, L. H. (1993). The tectonic expression slab pull at continental convergent boundaries. *Tectonics*, 12(2):303–325.

Rudnick, R. L. and Fountain, D. M. (1995). Nature and composition of the continental crust: a lower crustal perspective. *Reviews of geophysics*, 33(3):267–309.

Schellart, W. P. (2008). Overriding plate shortening and extension above subduction zones: A parametric study to explain formation of the andes mountains. *Geological Society of America Bulletin*, 120(11-12):1441–1454.

Schlunegger, F. and Kissling, E. (2015). Slab rollback orogeny in the alps and evolution of the swiss molasse basin. *Nature communications*, 6.

Schmid, S. M., Pfiffner, O., Froitzheim, N., Schönborn, G., and Kissling, E. (1996). Geophysical-geological transect and tectonic evolution of the swiss-italian alps. *Tectonics*, 15(5):1036–1064.

Schultz, R. (1995). Limits on strength and deformation properties of jointed basaltic rock masses. *Rock Mechanics and Rock Engineering*, 28(1):1–15.

Seno, T. (2009). Determination of the pore fluid pressure ratio at seismogenic megathrusts in subduction zones: Implications for strength of asperities and andean-type mountain building. *Journal of Geophysical Research: Solid Earth*, 114(B5).

Sibson, R. H. (1994). Crustal stress, faulting and fluid flow. *Geological Society, London, Special Publications*, 78(1):69–84.

Singer, J., Diehl, T., Husen, S., Kissling, E., and Duretz, T. (2014). Alpine lithosphere slab rollback causing lower crustal seismicity in northern foreland. *Earth and Planetary Science Letters*, 397:42–56.

Spada, M., Bianchi, I., Kissling, E., Agostinetti, N. P., and Wiemer, S. (2013). Combining controlled-source seismology and receiver function information to derive 3-D moho topography for italy. *Geophysical Journal International*, 194(2):1050–1068.

Turcotte, D. and Schubert, G. (2002). *Geodynamics*. Cambridge University Press.

Uyeda, S. and Kanamori, H. (1979). Back-arc opening and the mode of subduction. *Journal of Geophysical Research: Solid Earth*, 84(B3):1049–1061.

van Dinther, Y., Gerya, T., Dalguer, L., Mai, P. M., Morra, G., and Giardini, D. (2013). The seismic cycle at subduction thrusts: Insights from seismo-thermo-mechanical models. *Journal of Geophysical Research: Solid Earth*, 118(12):6183–6202.

van Dinther, Y., Morra, G., Funiciello, F., and Faccenna, C. (2010). Role of the overriding plate in the subduction process: Insights from numerical models. *Tectonophysics*, 484(1-4):74–86.

Van Heck, H. and Tackley, P. (2008). Planforms of self-consistently generated plates in 3d spherical geometry. *Geophysical Research Letters*, 35(19).

van Hunen, J. and Allen, M. B. (2011). Continental collision and slab break-off: a comparison of 3-d numerical models with observations. *Earth and Planetary Science Letters*, 302(1-2):27–37.

Wells, D. L. and Coppersmith, K. J. (1994). New empirical relationships among magnitude, rupture length, rupture width, rupture area, and surface displacement. *Bulletin of the seismological Society of America*, 84(4):974–1002.

Whipple, K. X. (2009). The influence of climate on the tectonic evolution of mountain belts. *Nature geoscience*, 2(2):97.

Willett, S. D. (2010). Late neogene erosion of the alps: A climate driver? *Annual Review of Earth and Planetary Sciences*, 38:411–437.